Time-of-flight PET based on high-quantum-efficiency multianode PMTs

고양자효율 다양극 광전자증배관을 이용한 비정시간 측정 가능 PET

2019 년 02 월

서울대학교 대학원

의과학과

손 정 환

A thesis of the Degree of Doctor of Philosophy

Time-of-flight PET based on high-quantum-efficiency multianode PMTs

고양자효율 다양극 광전자증배관을 이용한 비정시간 측정 가능 PET

February 2019

Department of Biomedical Sciences,

The Graduate School

Seoul National University

Jeong-Whan Son

Abstract

Time-of-flight PET based on high-quantum-efficiency multianode PMTs

Jeong-Whan Son

Department of Biomedical Sciences

The Graduate School

Seoul National University

In vivo imaging of physiological activities in molecular level has proven to be useful for diagnosing diseases in early stage. Positron emission tomography (PET) is a widely used molecular imaging technique that provides three-dimensional images of functional changes with high sensitivity by estimating the distribution of injected radiotracers. The advent of time-of-flight (TOF) PET scanners has dramatically improved the quality of generated images, which led to enhanced diagnostic power and/or reduced scan time or patient radiation dose. Herein, a prototype TOF PET scanner based on advanced high-quantum-efficiency multianode photomultiplier tubes (PMTs) is presented. Superior time performance of the scanner was demonstrated and

improvement of reconstructed images was confirmed from various phantom studies. Finally, our system was verified to be capable of serving as a demonstration system that provides experimental evidences of the benefits of excellent time performance and to be useful for validating the feasibility of new PET applications that have been traditionally challenging.

....

Contents

List of Figures

List of Tables

General Introduction

Conventionally, a detector block of time-of-flight (TOF) positron emission tomography (PET) scanners consisted of an array of pixelated scintillators coupled with multiple single- or four-channel photomultiplier tubes (PMTs) (e.g., block detectors or quadrant-sharing detectors) which can reduce the manufacturing cost because of the small number of photosensors (*1, 2*). However, the time performance of the PET detectors was significantly compromised because of the increased transit time jitter and enhanced loss of scintillation photons at the large gaps between the effective areas of PMTs.

Alternatively, there are two complementary approaches for improving the time performance of TOF PET detectors by utilizing the advanced photosensor technologies: silicon photomultipliers (SiPMs) and high-quantum-efficiency (high-QE) multianode PMTs. The compactness and fast time response of SiPMs make it suitable for developing TOF PET detector blocks (*3, 4*). The MRI-compatibility is another benefit of this solid-state photosensor (*5–7*). On the other hand, multianode PMTs are based on well-proven vacuum-tube technology, providing highly stable operation (e.g., less vulnerable to fluctuations of temperature and bias voltage) compared to SiPMs (*8*). The lower dark count rate (i.e., higher SNR) (*9*) and lower output capacitance of multianode PMTs are also suitable for developing TOF PET

scanners because the output signals can be multiplexed with higher ratio while not compromising the time performance. The better radiation hardness is another advantage of PMTs, which is required characteristics for a real-time charged-hadron therapy monitoring system (*10*).

The aim of this thesis is to develop a prototype TOF PET scanner with superior time performance based on the advanced multianode PMTs. Chapter 1 describes the advantages of using the high-QE multianode PMT as a photosensor and the development of TOF PET detectors. The optimization procedure of its timing resolution and performance of the PET detectors are presented. Chapter 2 shows the development of the prototype TOF PET scanner using the detectors described in Chapter 1 and the performance evaluation of the scanner according to National Electrical Manufacturers Association (NEMA) NU2-2007 standard (*11*). Finally, various phantom studies are presented to verify the improvement of image qualities because of the fine-time performance of the PET scanner.

Chapter 1. Development of TOF PET detectors

1.1. Background

To improve the timing performance of PET detectors, multianode PMTs with high-QE, low transit time spread, small pixel size, large effective area, high packing density (effective area/external size) and moderate cost are preferred. The H10966A-100 PMT is such an advanced multianode PMT equipped with super-bialkali (SBA) photocathode which provides higher blue sensitivity index (BSI) and QE (or higher number of generated photoelectrons) compared to the conventional and widely-used multianode PMTs (H8500) with bialkali (BA) photocathode. The fewer number of dynode stages of the H10966A-100 results in lower transit time and transit time spread. Also, it has been reported that the high-QE PMTs showed improved crystal identification ability (*12*).

In this chapter, TOF PET detector blocks based on the high-QE multianode PMTs were developed. The developed PET detectors were optimized to achieve the best time performance from the advanced PMTs. The optimal setup was applied to all detectors and the performance was evaluated.

1.2. Materials and Methods

1.2.1. Photomultiplier Tube

In this thesis, H10966A-100 PMT (Hamamatsu Photonics K. K., Japan) was used as a photosensor. The PMT has 64 anode channels (8×8) for positioning the detection location and 1 dynode channel for triggering. The photocathode material of H10966A-100 was SBA which yielded higher BSI (13.5) and higher QE (34.1% @420 nm) compared to conventional multianode PMTs equipped with BA photocathodes. The PMT is expected to show improved timing resolution because of reduced statistical error in consequence of the two factors: the higher QE and the lower transit time jitter owing to fewer number of dynode stages (i.e., 8 vs. 10–12) and lower transit time (i.e., 4 ns vs. 5.3–6 ns). Table 1.1 summarizes the main characteristics of several multianode PMTs with the same number of anode channels and the same dimensions provided by Hamamatsu Photonics K. K..

Table 1.1. Main characteristics of 8 × 8 Multianode PMTs from Hamamatsu Photonics K. K.

	H10966A-100	H10966	H12700	H8500
Photocathode	SBA	BA	BA	BA
BSI (Typ.)	13.5	9.5	12	9.5
QE (420 nm) (%)	34.1[a]	24	30.3[a]	24[a]
Dynode stages	8	8	10	12
Transit time (ns)	4	4	5.3	6
Transit time jitter (ps)	N/A[b]	N/A[b]	280	400
Gain (Typ.)	3.2×10^5	3.3×10^5	1.0×10^6	1.5×10^6
Dimension (mm^2)	52×52	52×52	52×52	52×52
Effective area (mm^2)	49×49	49×49	48.5×48.5	49×49
Anode size (mm^2)	5.8×5.8	5.8×5.8	6×6	5.8×5.8

[a] Calculated from the difference of quantum efficiency and blue sensitivity index of H10966 [b] No measured transit time jitter

1.2.2. Detector Design

Each PET detector consisted of a 15 × 15 array of LGSO ($Lu_{1.9}Gd_{0.1}SiO_4$:Ce, Hitachi Chemical Co., Japan) scintillators ($3 \times 3 \times 20$ mm^3) coupled with a H10966A-100 PMT using optical grease (BC-630, OKEN, Japan). The crystal pitch was 3.1 mm and the array size was $46.4 \times 46.4 \times 20$ mm^3. The scintillator block size was only slightly smaller than the effective area of the PMT (49×49 mm^2). Each crystal was chemically polished and covered with reflectors (ESR, 3M, USA) except for one surface contacting with the PMT window.

1.2.3. Front-end Electronics

Electronics such as a gain compensator, a charge division network, and amplifiers were implemented. A gain compensation circuit was used to adjust gain differences between anodes in a PMT (maximum/minimum gain ratio of up to 2.7) (*13*).

A resistor-based charge division network was used to multiplex the 64 gain-compensated anode signals into four position-encoded signals (A, B, C, and D) to reduce the number of signals (*14*). The interacted position can be decoded from the summed value (i.e., charge) of the four signals (Q_A, Q_B, Q_C, and Q_D) by using the equations shown below.

$$X = \frac{Q_A + Q_B - (Q_C + Q_D)}{Q_A + Q_B + Q_C + Q_D}$$

$$Y = \frac{Q_A - (Q_B + Q_C) + Q_D}{Q_A + Q_B + Q_C + Q_D}$$

The gamma-ray detection time was measured using a dynode signal. The dynode signal was amplified by an ultrahigh-speed (1.5 GHz bandwidth and 4100 V/μs slew rate) current feedback operational amplifier. If the dynode signal becomes higher than the predefined threshold voltage, a trigger signal was generated and transmitted to a time-to-digital converter (TDC).
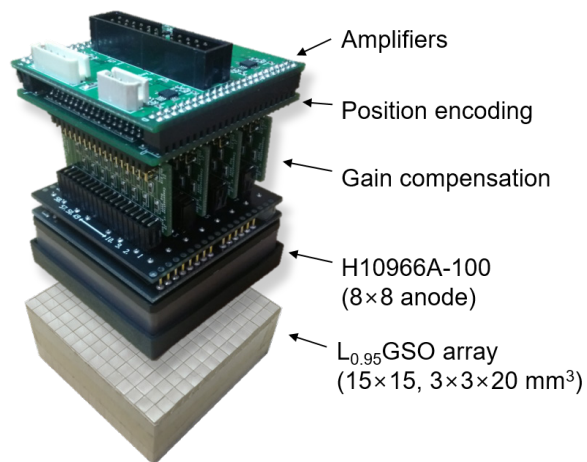
Figure 1.1. Developed TOF PET detector. Its modular design is suitable for building a PET scanner.

1.2.4. Data Acquisition

A time-to-digital converter (TDC) implemented in the field programmable gate array (FPGA; ML605, Xilinx, USA) was used to measure the gamma-ray detection time. The TDC has 47.5 ns latency, 12.8 ps measurement uncertainty, and 200 MSa/s maximum conversion rate (*15*). The detection time information was transmitted to the data acquisition (DAQ) system using high speed serial communication protocol.

The position-encoded signals were continuously digitized at 125 MHz and 12-bit resolution using analog-to-digital converters (ADS6425, Texas Instrument, USA). The digitized signals and detection time information generated from the TDC were acquired using an FPGA-based (ML605) DAQ system (*16*). Once receiving a trigger signal from the TDC, the position-encoded signals were integrated for 200 ns to obtain energy information (i.e., Q_A, Q_B, Q_C, and Q_D). The calculation was done in real time with the DAQ system. Then, the energy and detection time information formed the final data (128 bit/event) and the data was transferred to a personal computer via 1 Gbps Ethernet.

1.2.5. Experimental Setup

A reference detector consisting of a single-channel PMT (R9800, Hamamatsu Photonics K. K., Japan) coupled with a $4 \times 4 \times 10$ mm^3 LYSO (Lu$_{1.8}$Y$_{0.2}$SiO$_5$:Ce) scintillator was used to evaluate the performance of the developed PET detectors. A ^{22}Na point source (MMS06-22, Eckert & Ziegler, Germany) of 13.6 μCi was attached to the reference detector. The experimental setup was summarized in Figure 1.2.

The coincidence timing resolution of the pair of the developed detectors ($FWHM_{H10966A\text{-}100/H10966A\text{-}100}$) was calculated by correcting the contribution of the single timing resolution of the reference detector (STR_{REF}) from the measured timing resolution between the reference detector and the developed detector ($FWHM_{H10966A\text{-}100/REF}$) with the equation shown below. The single timing resolution of the reference detector was 255 ps.

$$FWHM_{H10966A-100/H10966A-100}$$

$$= \sqrt{2} \times \sqrt{FWHM_{H10966A-100/REF}^2 - STR_{REF}^2}$$
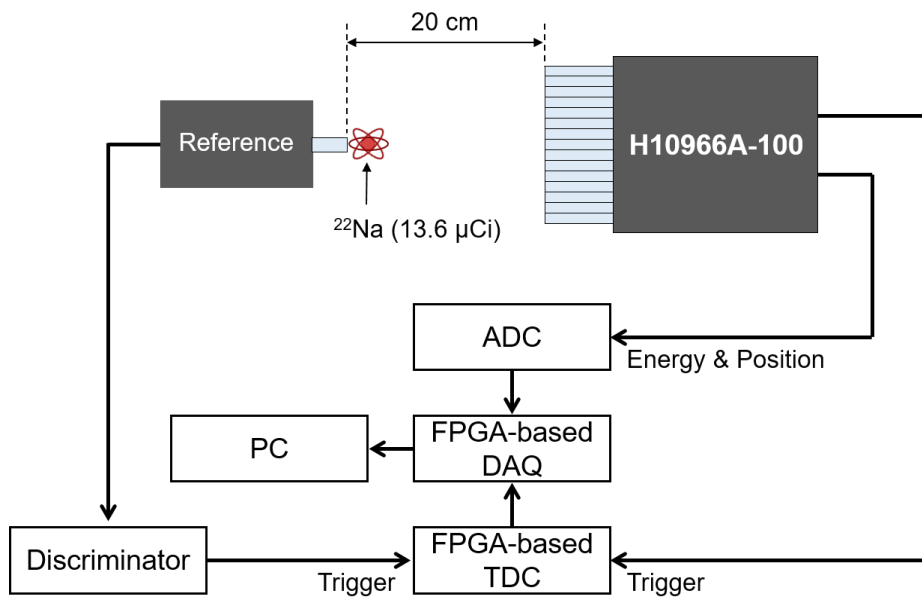
Figure 1.2. Experimental setup for coincidence data acquisition.

1.2.6. Analysis

A two-dimensional crystal map or a flood map was quantitatively evaluated by calculating the distance-to-width ratio (DWR). The DWR was determined as the ratio of the distance between the two adjacent peaks to the average full-width at half-maximum (FWHM) of the two peak distributions. The average DWR of N × M crystals is calculated from the following equation (*17*).

$$DWR_{avg} = \frac{1}{2NM - N - M} \left(\sum_{(i,j) \in (adj\ pairs)} \frac{distance(crystal_i, crystal_j)}{(FWHM_i + FWHM_j)/2} \right)$$

The energy resolution was calculated as the FWHM of a Gaussian fit to the 511-keV peak normalized by the peak. The timing resolution was calculated as the FWHM of a Gaussian function fitted to the histogram of the detection-time differences. The resolutions were estimated for individual crystals.

1.2.7. Timing Resolution Optimization

To achieve the best timing resolution of the PET detectors, three major parameters (i.e., bias voltage applied to a PMT, threshold voltage for generating trigger signals, and amplifier gain) were optimized. The coincidence timing resolution was measured with five different bias voltages (900, 950, 1000, 1050, and 1100 V) and five different threshold levels (3, 5, 7, 10, and 15% of the peak voltage of the average 511-keV dynode pulses). Then, with the optimal bias voltage and threshold level applied, the coincidence timing resolution was measured with different amplifier gains (from ×5 to ×95) using three randomly selected PMTs with different PMT gains (low, medium, and high gain). Finally, the average coincidence timing resolution of all 40 detectors were estimated with the optimal setup applied.

1.3. Results

1.3.1. Optimal Setup

The optimal parameter values were 1100 V bias voltage (i.e., the maximum voltage specified in the datasheet), 5% threshold level, and ×20 amplifier gain. Coincidence timing resolutions of the examined PET detectors with different parameter values were shown in Figure 1.3. Each point in the figure represents the average timing resolution of 15 × 15 scintillators in one detector. Although there is a concern that applying higher bias voltage than the recommended value by the manufacturer (1000 V) can cause increased dark count noise and shortened lifetime of a PMT, 1100 V was applied to PMTs in order to achieve the best time performance. If the recommended bias voltage (1000 V) is applied, approximately 20 ps degradation of timing resolution is expected as shown in Figure 1.3(b).
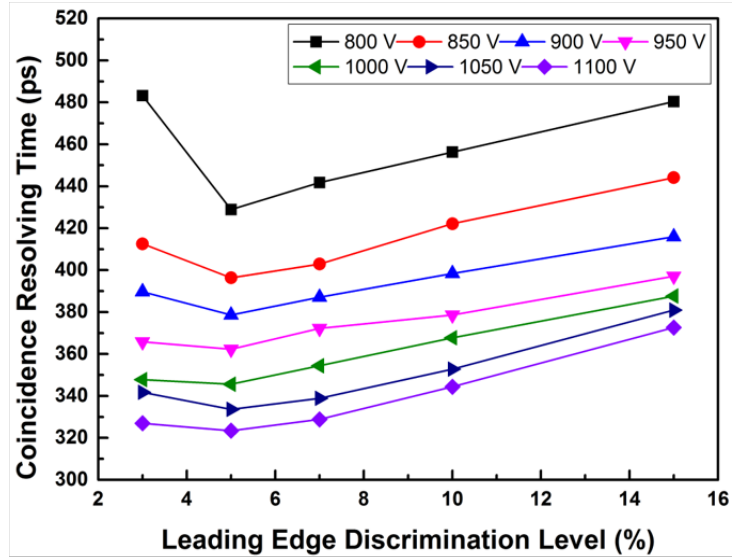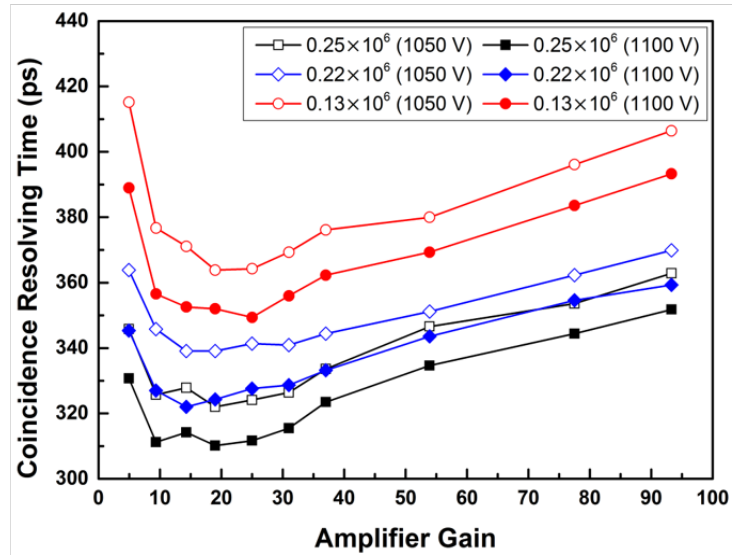
Figure 1.3. Coincidence resolving time (a) with different bias voltages and threshold levels (i.e., discrimination levels) and (b) with different amplifier gains using three randomly selected PMTs.

1.3.2. Detector Performance

All 15 × 15 scintillation crystals were clearly resolved in two-dimensional position histograms. The average DWR of 40 detectors was 5.3 ± 1.0. Considering the fact that the crystals generally can be separated from each other with the DWR value higher than 1, the developed PET detectors were demonstrated to be feasible for a high-resolution PET scanner. Representative flood map is shown in Figure 1.4.
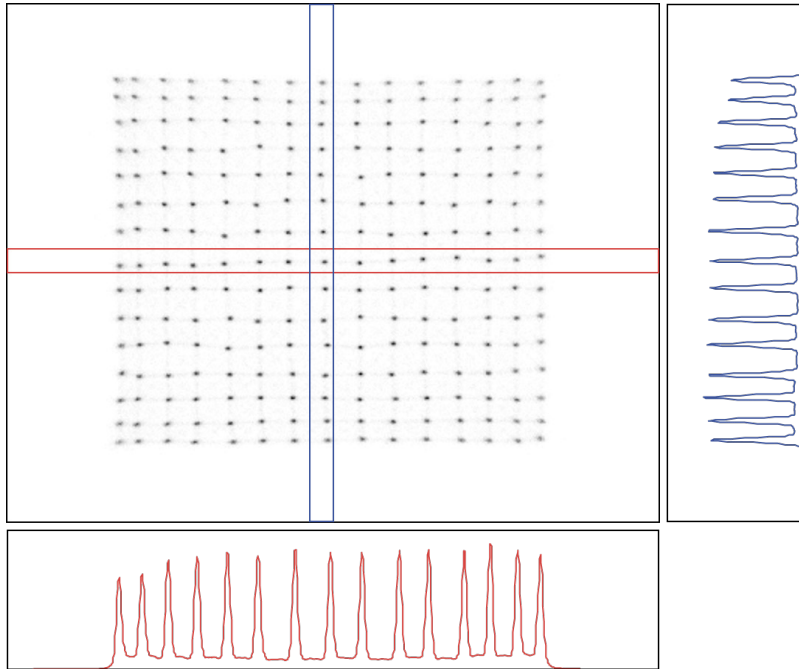
Figure 1.4. Representative flood histogram and its central vertical and horizontal profiles.

Representative histograms of coincidence timing resolutions, relative 511-keV photo-peaks, and energy resolutions of 15 × 15 LGSO crystals in a detector were shown in Figure 1.5.
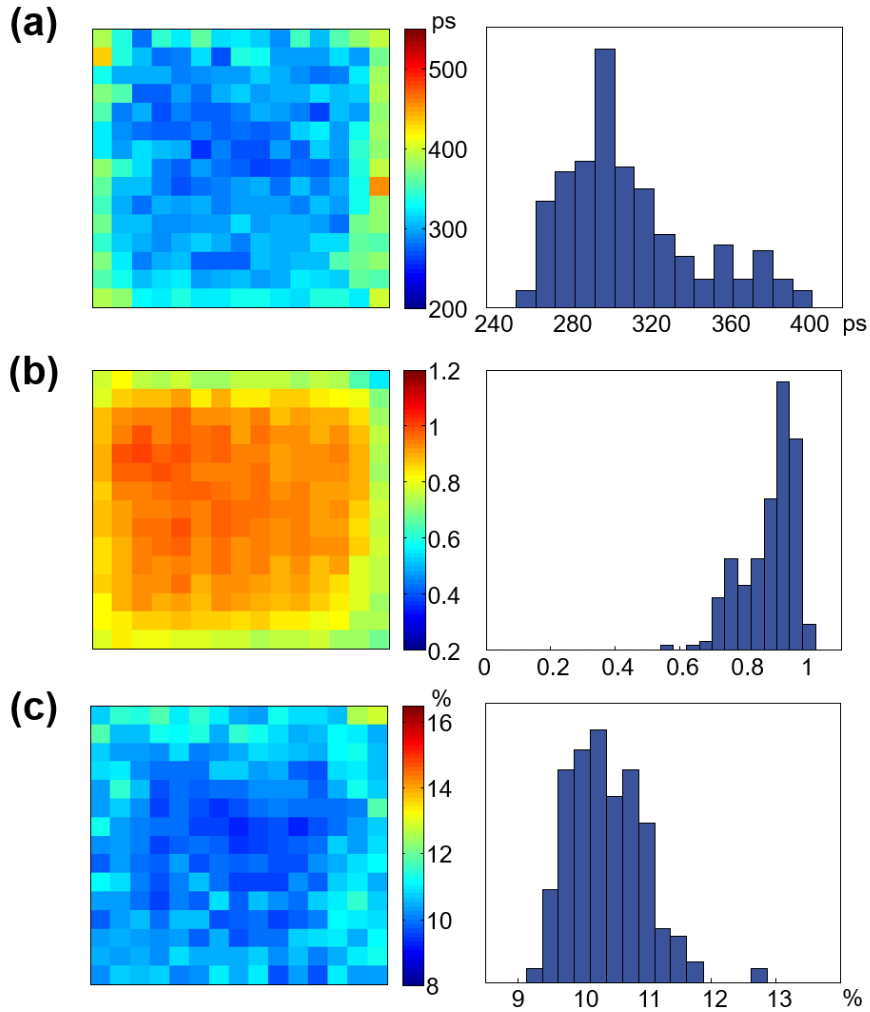
Figure 1.5. Representative two- and one-dimensional histograms of coincidence timing resolutions, normalized 511-keV peaks, and energy resolutions.

The average energy and timing resolutions were $11.04 \pm 0.8\%$ and 341 ± 45 ps, respectively. One-dimensional histograms of the resolutions were shown in Figure 1.6.

(a)

(b)
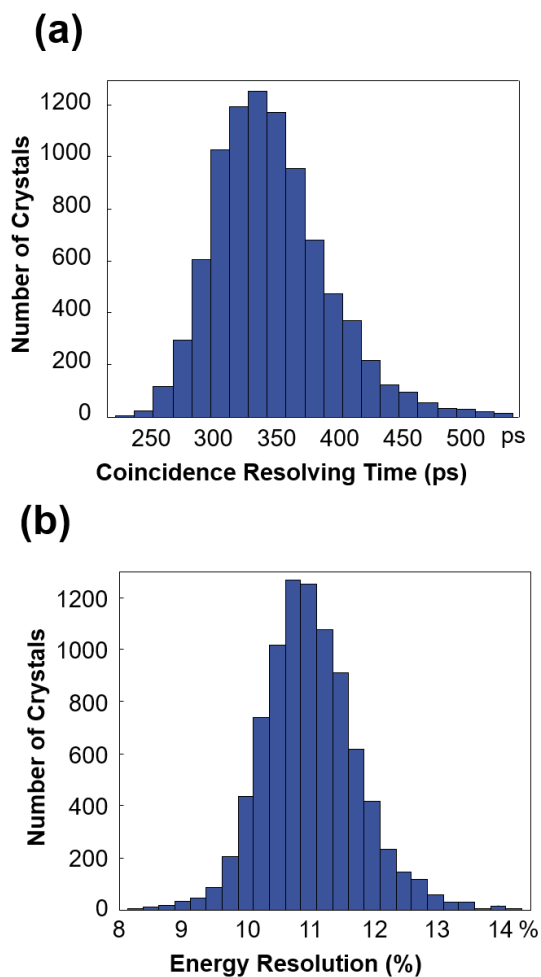
Figure 1.6. One-dimensional histograms of (a) the coincidence timing resolutions and (b) the energy resolutions for 9000 crystals of 40 PET detectors.

1.3.3. Verification of the Optimized Timing Resolution

It has been known that the product of the gain and collection efficiency (G·CE) and QE (or BSI) of PMTs are the two dominant factors affecting timing resolution of PET detectors (*18, 19*). In the references, it was reported that the CRT was inversely proportional to G·CE and BSI, respectively. By comparing the known tendencies with the relations obtained from the results of this study, it could be verified whether the time performance of the developed PET detectors was optimized.

Figure 1.7(a) shows the CRT and the inverse of the square root of G·CE·BSI of each developed PET detector. Also, the dependencies of the CRTs on each of G·CE and BSI were investigated by selecting only 15 detectors with similar BSI or G·CE respectively as shown in Figure 1.7(b) and Figure 1.7(c). In the figures, the proportional relationships were observed in accordance with the previous knowledge, indicating the developed PET detectors were well optimized.
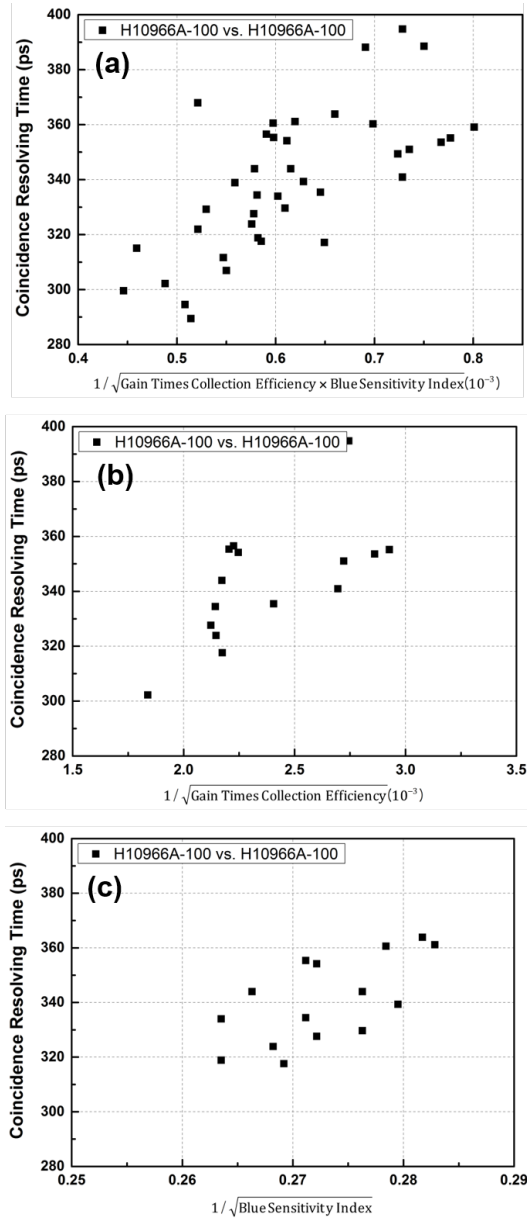
Figure 1.7. Dependency of coincidence timing resolutions on (a) G·CE·BSI for 40 detectors, (b) G·CE for 15 selected detectors with similar BSI, and (c) BSI for 15 selected detectors with similar G·CE.

1.4. Discussion

In this chapter, PET detector blocks based on the high-QE multianode PMTs, H10966A-100, coupled with LGSO scintillation crystals were described. Large effective area and small dead space of the PMT combined with compact front-end electronics allowed modular detector design which is suitable for flexible and extendible scanner design with moderate cost. The electronic parameters were optimized to yield the best timing resolution and to facilitate the advantages of excellent time performance of the PMT. The average coincidence timing resolution of 40 detectors was 341 ± 45 ps. The average energy resolution was $11.04 \pm 0.80\%$. The excellent energy resolution could further improve the time performance by narrowing the energy window without losing true events. The average DWR was 5.3 ± 1.0, which can be utilized for resolving more number of crystals (e.g., relative offset crystal blocks).

Recent studies using normal-QE multianode PMTs coupled with similar size of Lu-based crystals have shown timing resolutions as follows: 380 ps with 1 detector (7×7 array of $3 \times 3 \times 20$ mm^3 LGSO) (20), 442 ps with 48 detectors (16×16 array of $2.9 \times 2.9 \times 26(5+6+7+8)$ mm^3 LGSO) (21), and 415 ps with 1 detector (5×5 array of $3.2 \times 3.2 \times 25$ mm^3 LYSO) (22). The time performance obtained using the high-QE multianode PMTs in this study showed improved time performance compared to the results from normal-QE

PMTs. On the contrary, another study using a normal-QE multianode PMT with an array of LYSO scintillators (32 × 32 array of 1.5 × 1.5 × 15 mm^3) reported comparable timing resolution (i.e., 348 ps with 1 detector) (*23*). A limitation of this study is that the direct comparison of performance were not carried out between detectors based on normal-QE and high-QE PMTs.

Another studies have reported coincidence timing resolutions around 200 ps using single-anode PMTs coupled with fast scintillators (*18, 19, 24*). These studies achieved the superior results by shortening the transport length of scintillation photons to the PMTs, which was done through using short (~ 10 mm) scintillators (*18*) or attaching the side face of the scintillators to the PMTs rather than the end face (*19, 24*). However, these detector configurations are not suitable for building PET scanners because of the lower sensitivity and wider gap size between adjacent detector blocks. On the contrary, the clinical-sized scintillators (20 mm length) and the modular design of the developed detectors made the detectors suitable for building a PET system.

In the following chapter, a proof-of-concept prototype whole-body TOF PET scanner will be described consisting of the detector blocks developed in this chapter.

Chapter 2. Proof-of-concept prototype TOF PET system

2.1. Background

Chapter 2 describes a prototype whole-body TOF PET scanner based on the PET detectors introduced in Chapter 1. With the excellent timing resolution, smaller cross-section (3×3 mm^2) of scintillators compared to the size of widely used crystals (4×4 mm^2), and small gap size between adjacent detector blocks, the prototype TOF PET system achieved superior time performance and spatial resolution. The detailed scanner design and performance results were presented. Furthermore, the feasibility of the scanner as an experimental demonstration system for providing evidences of the benefits of fine-time performance was verified by conducting various phantom studies and investigating the known advantages of improved timing resolution (i.e., image quality enhancement, robustness to inconsistent and incomplete data, and improved performance of joint activity/attenuation estimation algorithms) under more clinically relevant condition (i.e., longer axial length (46.4 mm vs. 6.15 mm (*25*)) and practical scintillator selection (LGSO vs. LaBr3 (*26*))) compared to other PMT-based prototype TOF PET scanners with similar timing resolutions (*25, 26*).

2.2. Materials and Methods

2.2.1. Prototype TOF PET Scanner

The prototype scanner was developed using forty PET detectors developed in Chapter 1, yielding 641 mm diameter and 46 mm axial length. The transaxial field-of-view was 518 mm. Because the size of the crystal array (46.4×46.4 mm^2) was smaller than the effective area of the PMT (49×49 mm^2), the gaps between adjacent detectors were just smaller than the size of two crystals. The energy and coincidence time window were set to 435–590 keV and 4 ns, respectively. The position-encoded signals from every four detectors were multiplexed (i.e., 4:1 multiplexing ratio) by using a bipolar multiplexer to further reduce the number of readout channels (*27*). The FPGA-based 40-ch TDC and DAQ described in Chapter 1.2.4 were employed. Table 2.1 summarizes the main characteristics of the prototype PET scanner.
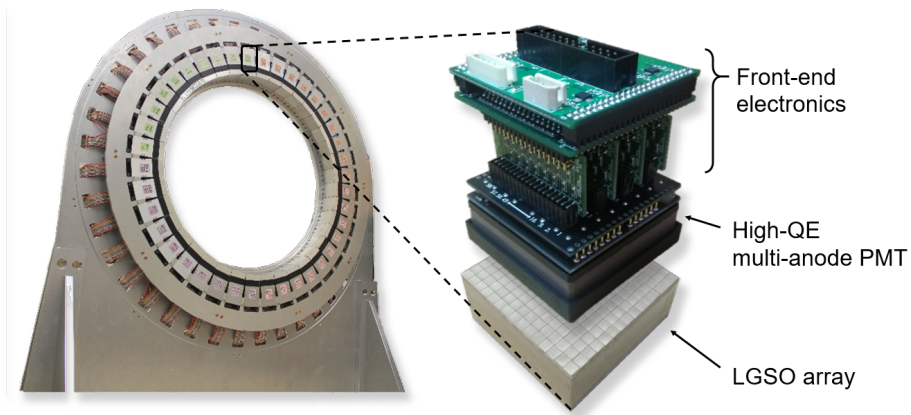
Figure 2.1. Prototype TOF PET scanner and its detector block.

Table 2.1. Main characteristics of the high-QE multianode PMT-based TOF PET scanner

Characteristics	Value
Crystal material	LGSO ($3\times3\times20$ mm^3)
Crystal pitch (mm)	3.1
Crystal array	15×15
# detector blocks	40
Transaxial field-of-view (mm)	518
Axial field-of-view (mm)	46.4
Energy window (keV)	435–590
Time window (ns)	±2

2.2.2. System Performance Measurement

To measure the scanner-level energy, timing, and spatial resolutions, coincidence data were acquired using a ^{22}Na point source located at the center of the scanner. The system-level flood map quality was evaluated by calculating the DWR as described in Chapter 1.2.6. The energy and timing resolutions were calculated from the FWHM of Gaussian functions fitted to histograms as described in Chapter 1.2.6. The spatial resolutions were measured at two different source positions (i.e., at 1 and 10 cm away from the center in the transverse direction while maintaining the axial location at the center). Two different reconstruction algorithms were used for the measurement of the spatial resolutions: the two-dimensional filtered back-projection (2D FBP) and the three-dimensional ordered-subset expectation-maximization (3D OSEM) algorithm (1 iteration and 15 subsets). The matrix size of the reconstructed images was $512 \times 512 \times 29$ with a voxel size of $0.8 \times 0.8 \times 1.55$ mm^3. The analysis method specified in NEMA NU2-2007 was followed to calculate the spatial resolutions (*11*). The sensitivity and count-rate performance of the scanner were evaluated according to the NEMA NU2-2007 protocol although limited performance was expected because of the short axial length of the system.

2.2.3. Image Quality Measurement

To evaluate the image quality of the prototype scanner, NEMA International Electrotechnical Commision (IEC) body phantom was scanned. The phantom was filled with ^{18}F solution and the background activity concentration was 5.3 kBq/ml. The concentration of the hot lesions was four times higher than that of the background. The number of the acquired coincidence events was 48 million. The improvement owing to the excellent time performance of the scanner was demonstrated by comparing the reconstructed images with and without TOF modeling.

Reconstruction algorithm was 3D list-mode OSEM with 15 subsets, 5 iterations, a 5-mm (FWHM) transaxial postfilter, and a 3-mm axial postfilter for both TOF and non-TOF reconstructions. The number of iterations was determined to 5 at which contrast recovery coefficient of the reconstructed body phantom image was converged. The matrix size of the reconstructed images was $128 \times 128 \times 29$ with a voxel size of $3.1 \times 3.1 \times 1.55$ mm^3.

Attenuation correction was done using a registered computed tomography (CT) image that was taken from a commercial PET/CT scanner (Biograph mCT64, Siemens Medical Solutions, USA). Component-based normalization was done using the factors derived from the acquired data of ^{68}Ge quality-control phantom (EG-0318-2.5M; Eckert & Ziegler, Germany). The number of random events were estimated using the singles rate. The distribution of

scattered events was obtained from GATE Monte Carlo simulation of the prototype scanner and the body phantom. Because of the incompleteness of scatter estimation, the scale of the simulated scatter distribution was adjusted by fitting the tail parts of simulated and measured sinograms.

To quantitatively evaluate the image quality, the contrast recovery coefficient (CRC) and background variability (BV) of each sphere of the body phantom were calculated according to the NEMA NU2-2007 protocol. However, because of the short axial length, the background regions-of-interest were drawn at the $\pm$ 1.5 cm away from the central slice rather than $\pm$ 2 cm which was specified value in the protocol. In addition, lung residual error was measured.

2.2.4. Robustness to Errors in Data Correction

The body phantom images were reconstructed without applying one of the attenuation, normalization, and scatter corrections to evaluate the robustness of the prototype scanner to data correction errors. In addition, the image was reconstructed using a radially 10-mm shifted attenuation map to investigate the effects of attenuation map mismatch due to patient breathing or movement. The amount of the shift was determined to 10 mm because the average movement of organs including lung, liver, diaphragm, and pancreas is about 10 mm (*28*).

2.2.5. Partial Ring Geometry and Limited Angle Tomography

The improvement of the images because of the fine-timing resolution in case of limited angle tomography was examined. The body phantom images were reconstructed using the list-mode data from which certain detector data were removed. Two different partial ring geometries were investigated.

The first geometry was the split-ring geometry, which can be used to scan the breast with shorter distance between two C-shaped partial rings as shown in Figure 2.2(a) (*29*). This geometry is also used to combine the PET system with hadron-therapy instruments (*30*). In the prototype scanner, 10 detectors were removed (i.e., 25%) to form 140-mm wide gap between the two C-shaped partial rings which was wide enough for a beam delivery system to be located in the scanner (*30*).

The second geometry was the sparse-ring geometry, which can be used to reduce the scanner cost or to extend the axial length without increasing the cost as shown in Figure 2.2(b). In this study, the detectors were regularly removed to maximize gap artifacts in the reconstructed images due to the incomplete data sampling. In the same manner as the first geometry, 10 detectors were removed.

To compare the artifacts in the background region, a background uniformity (BU) was defined as the standard deviation divided by the mean of

the background intensities. BV was not used here because it cannot reflect overall background artifacts.
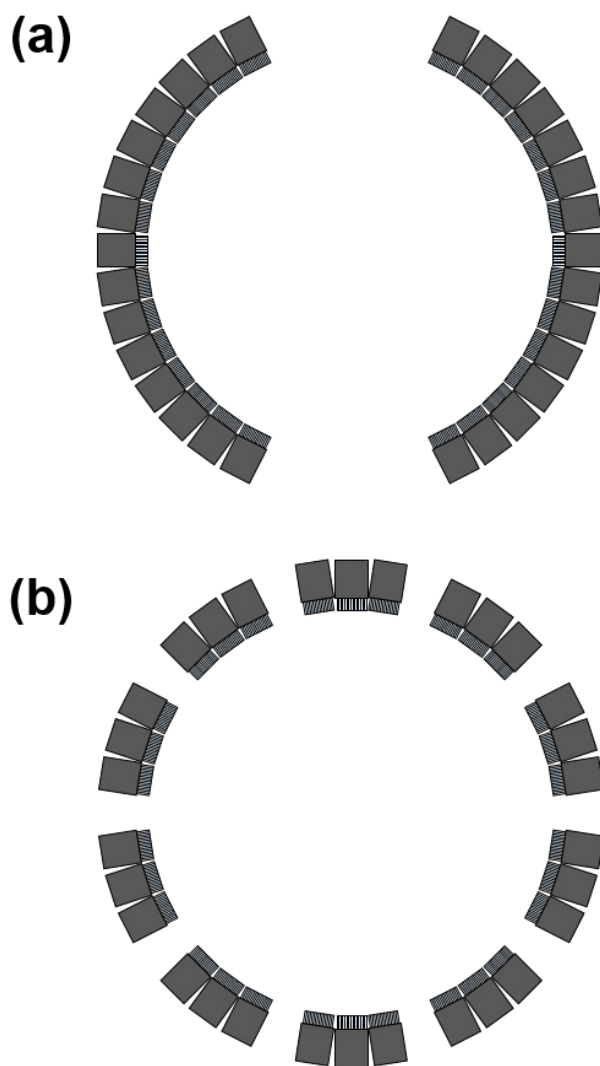
Figure 2.2. Partial ring geometries for limited angle tomography. (a) Split-ring geometry and (b) sparse-ring geometry.

2.2.6. Joint Estimation of Activity and Attenuation

The performance enhancement of joint activity and attenuation reconstruction algorithms with a 360-ps timing resolution was demonstrated. The IEC body phantom data was reconstructed using two commonly used joint estimation algorithms.

The first joint estimation algorithm was the maximum-likelihood activity and attenuation estimation (MLAA), which executed the maximum-likelihood expectation maximization and the maximum-likelihood transmission tomography equations back and forth to jointly update activity and attenuation images (*31*). In each iteration, total counts were scaled with a constant determined from a prior of zero attenuation values outside of the phantom contours.

The second algorithm was the maximum-likelihood activity and attenuation correction factor (MLACF), which determined the attenuation correction factor without reconstructing the attenuation map to achieve faster convergence rate and lower computation complexity than MLAA (*32*). Total counts were scaled using a prior of the known total activity.

For both algorithms, the number of subsets and iterations were 15 and 5, respectively. The subiteration ratio between the activity and attenuation updates was 1:1.

The scatter distribution was obtained from GATE Monte Carlo simulation, which is not feasible in routine scans. However, to solely investigate the performance improvement of joint estimation algorithms because of the 360-ps timing resolution, data correction including scatter correction was assumed to be performed correctly.

2.2.7. Comparison to Conventional 600-ps TOF PET

The improvement of images from 360 ps timing resolution compared to the conventional 600 ps timing resolution was demonstrated by comparing the images reconstructed with different timing resolutions (i.e., 360 and 600 ps) using the same data used in Chapters 2.2.4–2.2.6. The timing resolution of acquired data was degraded to 600 ps by adding Gaussian noise to the detection time information.

2.3. Results

2.3.1. System Performance Measurement

The scanner-level energy and coincidence timing resolutions were 13.67 ± 1.48% and 360 ± 26 ps, respectively. The histograms of energy and coincidence timing resolutions were shown in Figure 2.3.
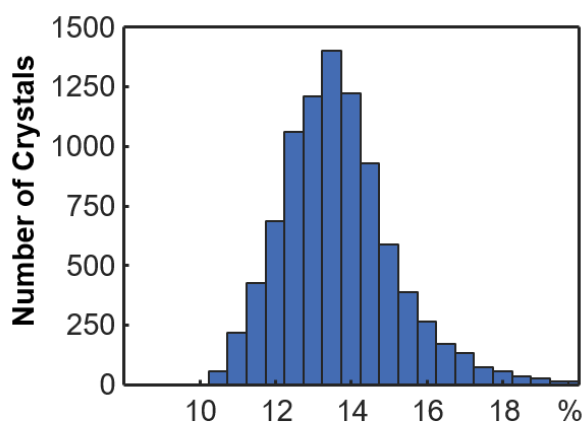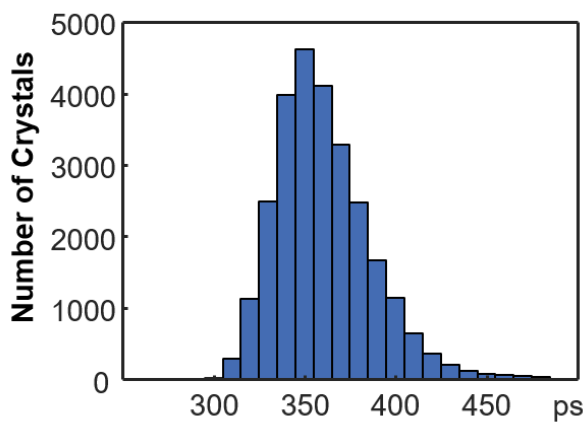
Figure 2.3. One-dimensional histograms of energy resolutions and coincidence resolving times.

The average DWR was 3.8 ± 0.7. The representative flood histograms were shown in Figure 2.4.
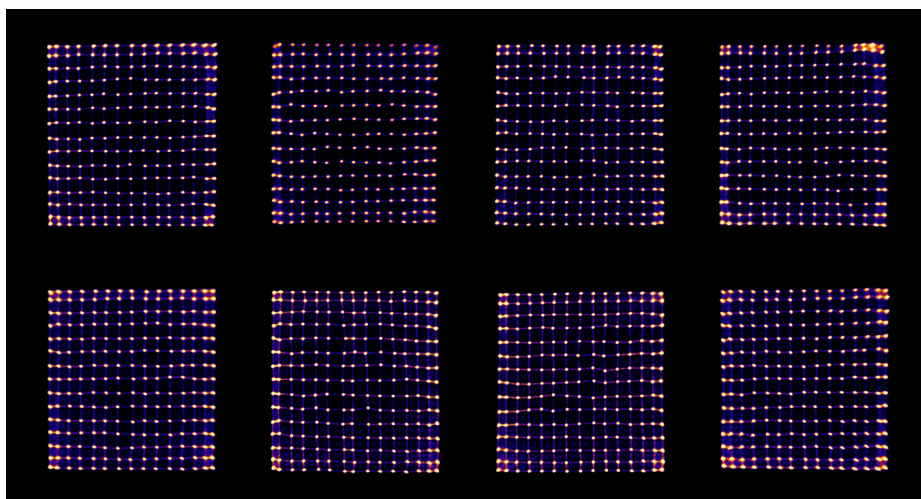
Figure 2.4. Representative flood histograms of the TOF PET scanner.

The transverse spatial resolutions at 1 cm off-center location were 3.5 mm with the 2D FBP algorithm and 2.0 mm with the 3D OSEM algorithm. The average transverse spatial resolutions at 10 cm off-center location were 4.1 mm with the 2D FBP algorithm and 2.7 mm with the 3D OSEM algorithm. The transverse and axial spatial resolutions were summarized in Table 2.2.

Table 2.2. Spatial resolution of the TOF PET scanner

	Radial position: r = 1 cm		Radial position: r = 10 cm		
	Transaxial	Axial	Tangential	Radial	Axial
2D FBP					
FWHM (mm)	3.5	2.7	3.7	4.5	3.9
FWTM (mm)	7.9	6.1	7.7	8.8	6.7
3D OSEM					
FWHM (mm)	2.0	2.4	2.3	3.2	3.1
FWTM (mm)	4.4	5.2	4.7	6.2	6.3

The sensitivity of the prototype scanner was 385 cps/MBq at the center and 404 cps/MBq at 10 cm off-center. The peak noise equivalent count rate was 838 cps at 2.31 KBq/ml. The peak true count rate was 1430 cps at 2.97 kBq/ml. The sensitivity and count rate performance were shown in Figure 2.5.
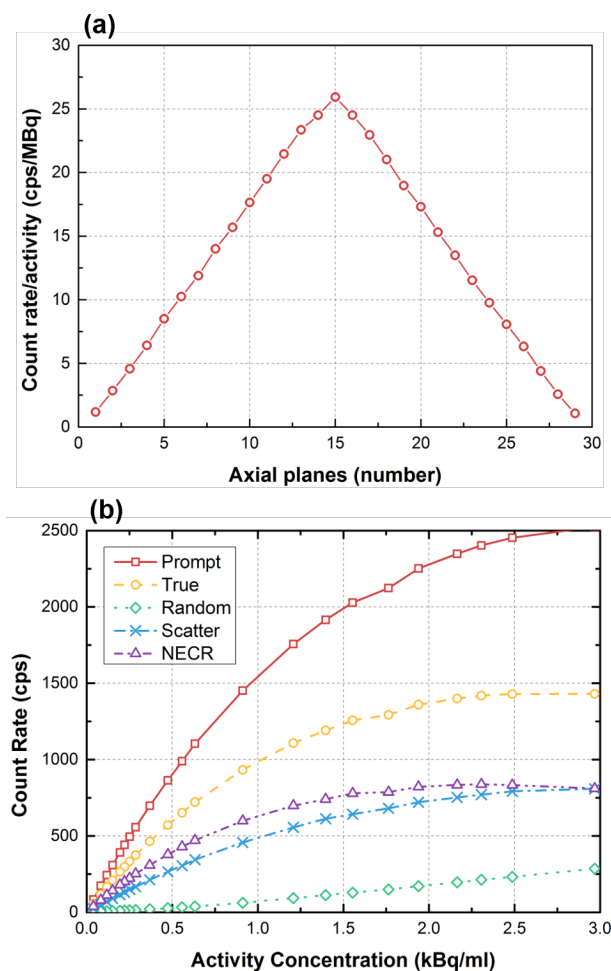
Figure 2.5. (a) Axial sensitivity profile and (b) count rate as a function of activity concentration.

2.3.2. Image Quality Measurement

The TOF image showed better background uniformity and less artifacts than the non-TOF image as shown in Figure 2.6. Although the CRCs of the hot lesions were similar (less than 3% difference in average), the CRCs of the cold lesions in the TOF image were higher (more than 10% in average) than those in the non-TOF image. The BVs of the TOF image were lower than those of the non-TOF image in every size of spheres (more than 13% in average). The lung residual errors were $9.2 \pm 0.7\%$ and $14.8 \pm 2.4\%$ in the TOF and non-TOF images, respectively. The reconstructed body phantom images, one-dimensional profiles, CRCs and BVs of the TOF and non-TOF data were shown in Figures 2.6 and 2.7.
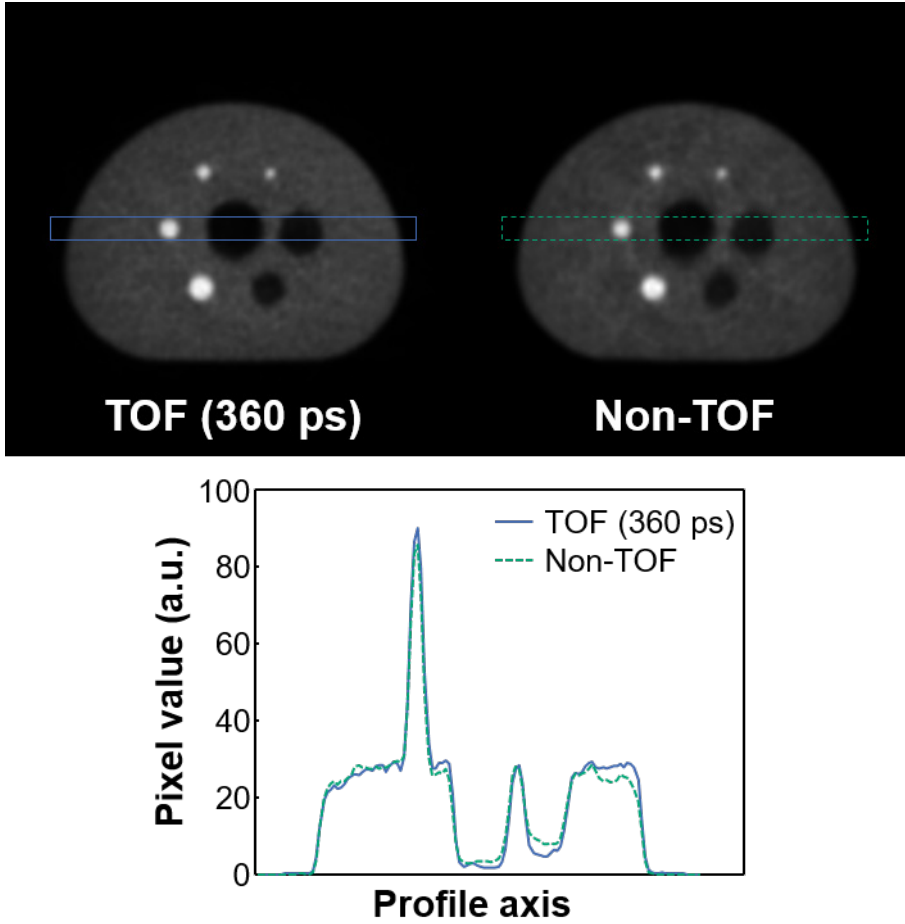
Figure 2.6. Reconstructed body phantom images with and without TOF information (top) and their profiles across the center of the phantom (bottom).
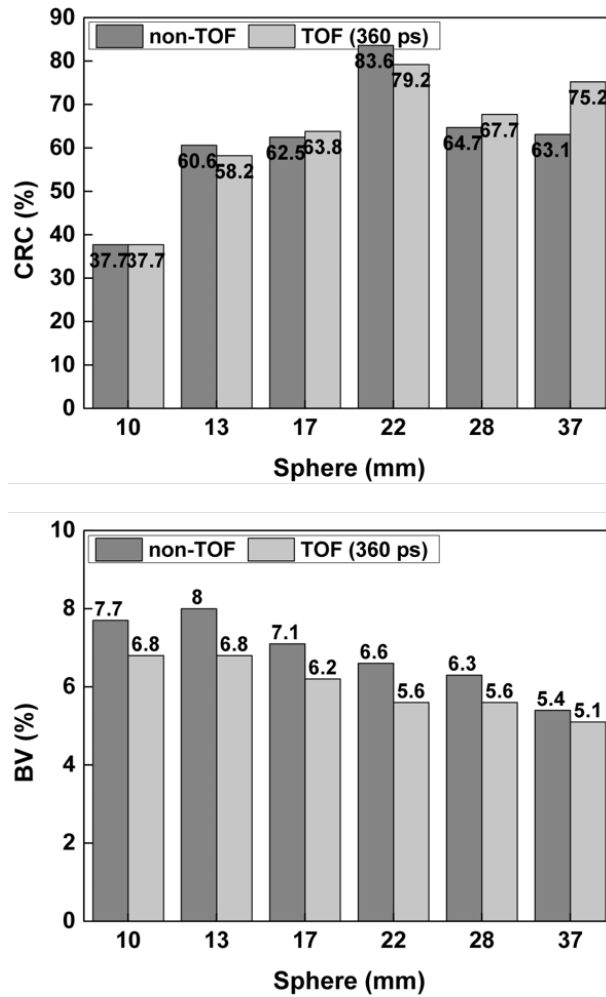
Figure 2.7. CRCs and BVs of each sphere in the body phantom.
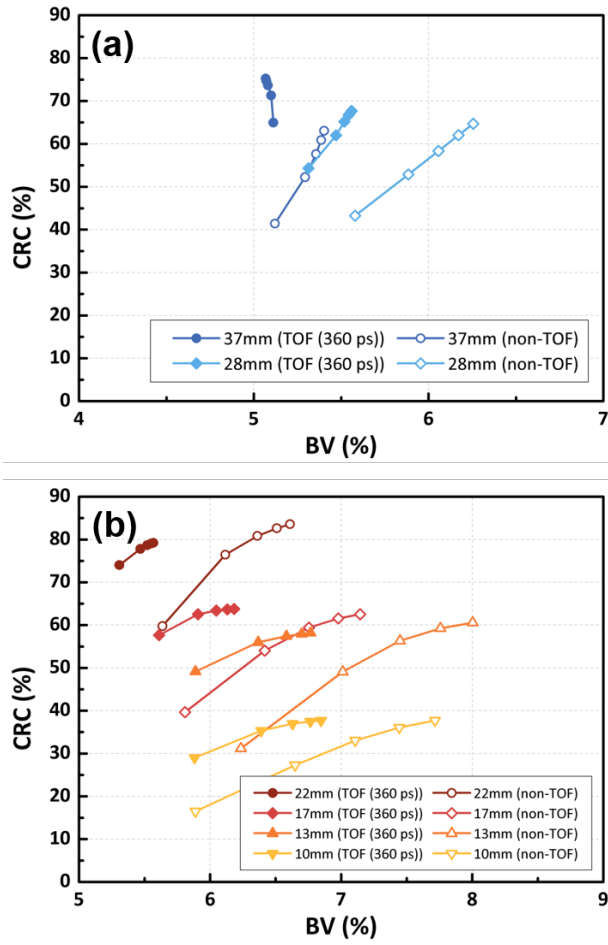
Figure 2.8. CRCs and BVs with different number of iterations (1–5) for (a) cold spheres and (b) hot spheres.

2.3.3. Robustness to Errors in Data Correction

Without applying attenuation correction, the non-TOF image showed overestimated activity concentration near the phantom surface and in the lung region and severe depth-dependent activity underestimation. On the contrary, the TOF image (360 ps) presented strong robustness to the attenuation artifacts. Only slight over- and underestimation of activity concentration were observed. The activity of the lung insert was three times lower in the TOF (360 ps) image compared to the non-TOF image. The images reconstructed without employing attenuation correction were shown in Figure 2.9(a).

The results of mismatch between the activity image and the attenuation map were shown in Figure 2.9(b). The activity overestimation was observed at lower right side of the lung insert (indicated by arrows in the figures). However, the magnitude of the overestimation was 42% lower in the TOF (360 ps) image.

In case of no scatter correction, reduced contrast at cold spheres and overestimated activity around the center of the phantom were shown in the non-TOF image. The image distortion was greatly mitigated in the TOF image as shown in Figure 2.9(c).

Without normalization correction, severe circular saw-tooth artifacts were observed in the non-TOF image. However, these artifacts almost completely disappeared in the TOF image as shown in Figure 2.9(d).

The TOF images with the conventional timing resolution (600 ps) showed reduced image artifacts compared to the non-TOF images. However, the image artifacts were still noticeable (e.g., overestimation of activity concentration in the lung insert in Figure 2.9(a) and severe circular saw-tooth patterns in Figure 2.9(d)) in the 600-ps TOF images. In the 360-ps TOF images, the image distortions were largely mitigated, which demonstrated the improvement of the developed 360 ps timing resolution.
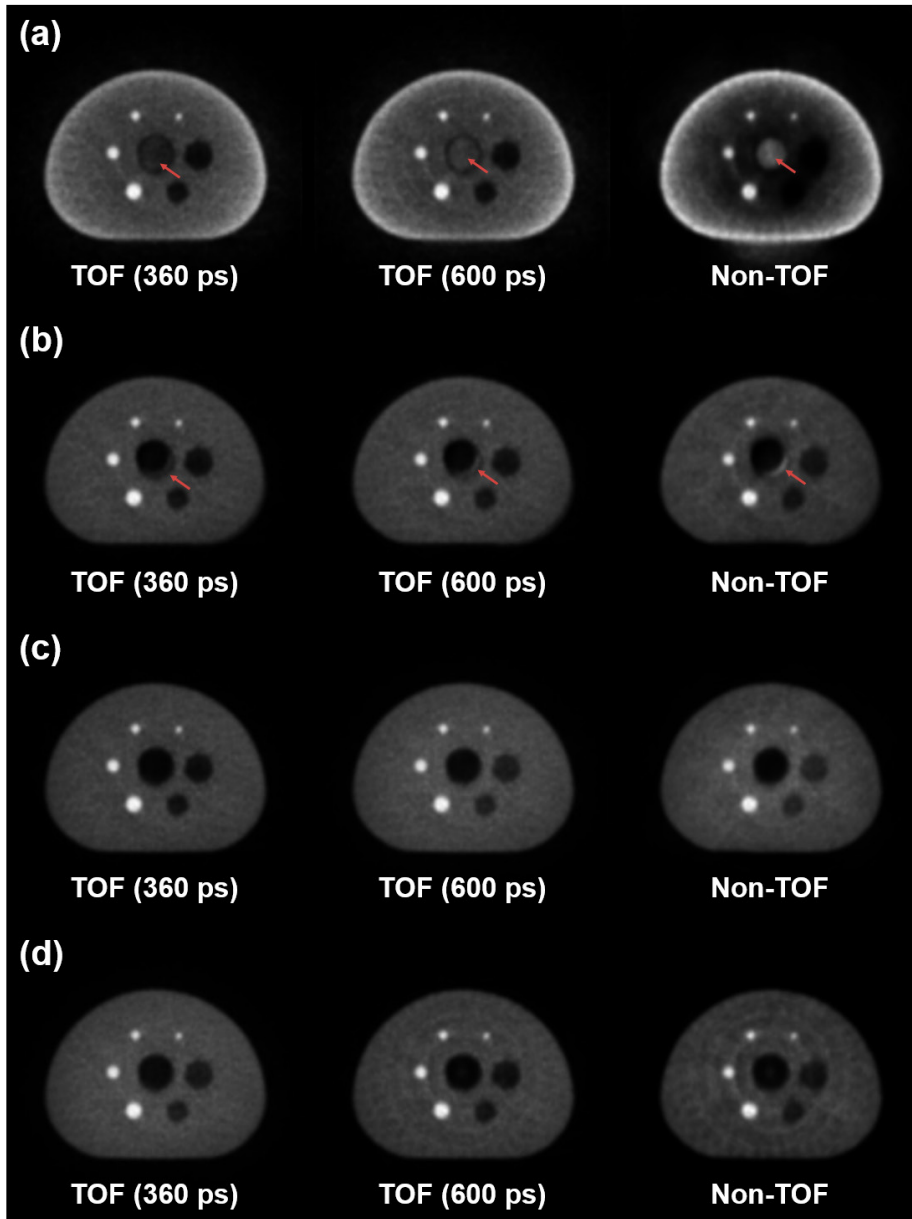
Figure 2.9. Reconstructed phantom images without applying one of the data corrections: (a) without attenuation correction, (b) with shifted attenuation map applied, (c) without scatter correction, and (d) without normalization.

2.3.4. Partial Ring Geometry and Limited Angle Tomography

In the split-ring geometry, the truncation artifact at the left and right sides of the body phantom became worse with TOF reconstruction. The BU was 21.0 with 360 ps timing resolution and 16.9 without TOF reconstruction. However, near the center of the phantom, the TOF images of both partial ring geometries showed significantly less artifacts compared to the non-TOF images. The image quality was slightly improved in the 360 ps timing resolution than 600 ps timing resolution. In the sparse-ring geometry, the BU of the 360-ps timing resolution image (12.5) was even comparable to that of the full-ring geometry without TOF (11.2). In summary, the excellent timing resolution of the prototype TOF PET system showed the reduced image distortions in the partial ring geometries as shown in Figure 2.10.
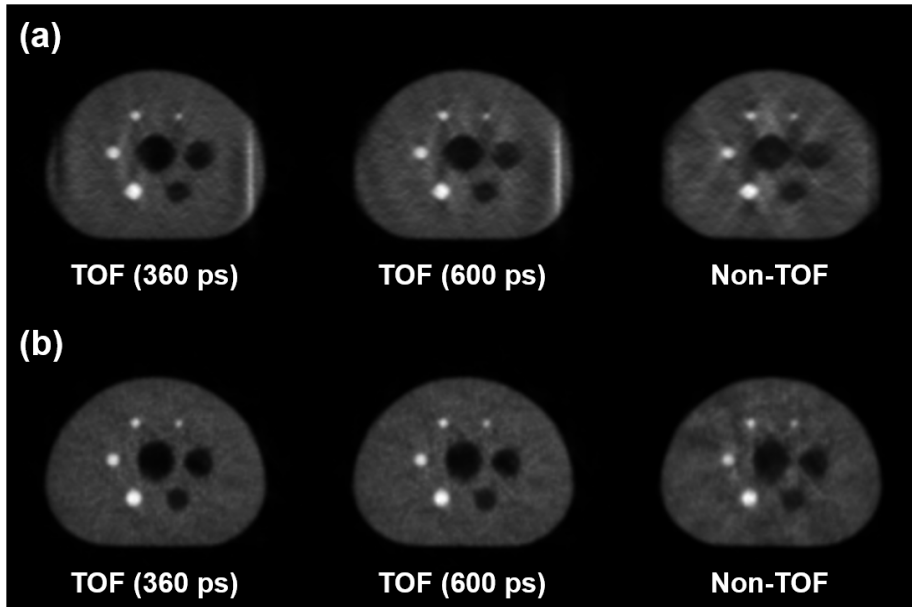
Figure 2.10. Phantom images reconstructed from (a) split-ring geometry and (b) sparse-ring geometry.

2.3.5. Joint Estimation of Activity and Attenuation

For both MLAA and MLACF algorithms, the accuracy of the activity and attenuation estimation was remarkably improved using 360 ps TOF information as shown in Figure 2.11. The activity images reconstructed with 360 ps timing resolution were almost comparable to the image corrected for the attenuation effect using CT data and reconstructed using the 3D OSEM algorithm. However, the jointly estimated activity images showed slightly higher noise and relatively overestimated activity concentration at the right side of the body phantom. In the MLAA algorithm, the crosstalk artifact at the lung insert and spheres were considerably reduced by including TOF information in the reconstruction as shown in Figure 2.11(a). In the MLACF algorithm, the reasonable activity image was obtained only if TOF information was included in the reconstruction as shown in Figure 2.11(b). The image artifacts such as higher noise level, overestimation, and crosstalk were mitigated in the 360-ps TOF images compared to the 600-ps images.
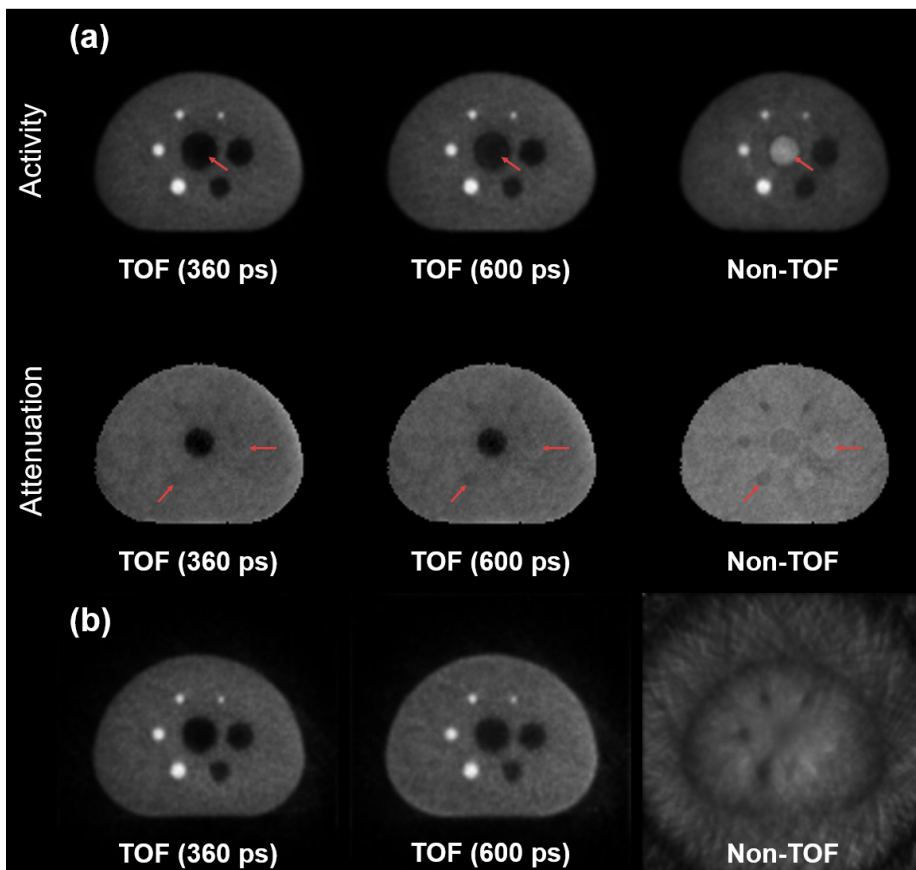
Figure 2.11. (a) Reconstructed activity images (up) and attenuation images (down) obtained using MLAA algorithm. (b) Reconstructed activity images using MLACF algorithm.

2.4. Discussion

In this chapter, a prototype TOF PET scanner based on advanced high-QE multianode PMTs and scintillation crystals with smaller cross section (3×3 mm^2) than the scintillators used in most current clinical PET scanners (4×4 mm^2) was described. The developed PET system achieved superior performance: 360 ps coincidence timing resolution, 13.7% energy resolution, and 3.1/2.2 mm spatial resolution using FBP/OSEM algorithms respectively. Then, the benefits owing to the fine-time performance was demonstrated using several known methods: improvement on BVs while maintaining CRCs of the body phantom image, robustness to inconsistent physical correction factors, robustness to incompletely sampled data, and better image quality from joint estimation algorithms. Also, the improvement of TOF images compared to the images reconstructed using conventional timing resolution (600 ps) was demonstrated.

The intrinsic performance obtained using the PET scanner was slightly degraded from the results of 40 detectors described in Chapter 1: 341 ps vs. 360 ps timing resolution, 11.0% vs. 13.7% energy resolution, and 5.3 vs. 3.8 DWR. The addition of multiplexing circuit (*27*) to the PET scanner was one of the reasons for the performance degradation. The signal-to-noise ratio of position-encoded signals was reduced because of the multiplexing, which led to degraded energy performance and crystal identification ability. Another

reason for the degradation was that the light coupling efficiency between the scintillators and the PMTs was decreased because of the aged optical grease.

The performance of widely-used clinical whole-body TOF PET scanners based on PMTs and Lu-based scintillators are as follows: 528 ps timing resolution, 11.5% energy resolution, and 4.1 mm spatial resolution with 4×4 mm^2 cross section (*1*), and 544 ps, 12.4%, and 4.7 mm with 4.2×6.3 mm^2 cross section (*33*). The SiPM-based whole-body clinical PET scanners presented improved time performance: 316 ps, 11.1% and 4.11 mm with 4×4 mm^2 cross section (*34*) and 390 ps, 10.5%, and 4.3 mm with 4×5.3 mm^2 cross section (*35*). The developed prototype scanner showed superior time performance (i.e., 360 ps) and spatial resolution (i.e., 3.5 mm) and comparable energy resolution (i.e., 13.7%) despite of smaller crystal dimension (i.e., 3×3 mm^2). Compared with single-channel PMT-based prototype PET scanners with similar timing resolutions (i.e., 314 ps, 19.6%, and 5.1 mm with 6.15×6.15 mm^2 cross section (*25*) and 375 ps, 6.5%, and 5.8 mm with 4×4 mm^2 cross section (*26*)), the developed PET scanner showed improved spatial resolution owing to the higher number of readout channels per each PMT (i.e., 8×8).

The time performance of the prototype PET scanner can be further enhanced by utilizing the state-of-the-art features of advanced scintillators, multianode PMTs and light coupling techniques. The fast version of LGSOs

(0.025%Ce) and Ca-codoped LSOs (0.4%Ca) are excellent alternatives because of their high scintillation output (i.e., > 30 k photons/MeV) and fast decay time (i.e., ~ 30 ns), which achieved 120 ps ($2.9 \times 2.9 \times 20$ mm^3) (*4*) and 140 ps ($2 \times 2 \times 20$ mm^3) (*36*) timing resolutions, respectively. Another good candidates are the scintillators generating prompt photons such as CdSe nanoplates (*37*) and ZnO:Ga nanocrystals (*38*) because of the considerably faster emission rate of prompt photons compared to the scintillation emission rate. Regarding multianode PMTs, replacing the photocathode material with ultra-bialkali (i.e., QE higher than 40%) can enhance the time performance (*20*). In addition, the dynode structure optimized to detection of single photons (*39*) has potential to improve timing resolution by resolving a single prompt photon from the advanced scintillators described earlier. The light coupling efficiency between scintillators and photosensors can be improved by applying nanostructures (i.e., photonic crystal) on the exit surface of the scintillators (*40*). The improved photo-statistics and the increased number of detected early-phase photons can enhance the time performance of the PET scanner.

The limitation of the prototype TOF PET scanner was its short axial length which led to limited sensitivity and count rate performance. The phantoms should be scanned for long time to acquire sufficient number of coincidence pairs. The sensitivity and count rate performance can be improved by adding detector rings and extending axial coverage of the PET scanner. The count

rate performance can be further enhanced by removing the multiplexing circuit from the scanner.

General Discussion

One of the technical approaches for improving the image quality of PET systems is to develop TOF PET scanners with better timing resolution. However, the conventional configuration of TOF PET detector blocks had structural limitations. This work was motivated by the goals to develop a proof-of-concept whole-body TOF PET scanner with superior time performance using the advanced multianode PMTs.

The developed prototype TOF PET scanner showed much improved timing resolution compared to the conventional commercial TOF PET scanners. To compare with the recent state-of-the-art SiPM-based TOF PET systems, our system showed similar time performance and better spatial resolution. Furthermore, the enhancement of image quality due to the improved time performance was experimentally demonstrated from various phantom studies.

Our system was verified to be capable of serving as a demonstration system that provides experimental evidences of the benefits owing to the fine-time performance. It will be useful for demonstrating the feasibility of new PET applications that have been traditionally challenging such as reconstructing images from few true counts (*41*) or mitigating image distortion (*29*). Moreover, the prototype PET scanner can be used to improve the advanced image reconstruction algorithms such as accelerating convergence rate and

reducing crosstalk artifacts in joint estimation algorithm (*42*) and mitigating

gap artifact in sparse PET geometries (*43*).

Reference

1. Jakoby BW, Bercier Y, Conti M, Casey ME, Berdriem B, Townsend DW. Physical and clinical performance of the mCT time-of-flight PET/CT scanner. Phys Med Biol. 2011 Apr; 56(8):2375–2389.

2. Wong W-H, Li H, Zhang Y, Ramirez R, An S, Wang C, et al. A high-resolution time-of-flight clinical PET detection system using a gapless PMT-quadrant-sharing method. IEEE Trans Nucl Sci. 2015 Oct; 62(5):2067–2074.

3. Schaart DR, Seifert S, Vinke R, van Dam HT, Dendooven P, Löhner H, et al. LaBr3:Ce and SiPMs for time-of-flight PET: achieving 100 ps coincidence resolving time. Phys Med Biol. 2010 Apr; 55(7):N179–N189.

4. Cates JW, Levin CS. Advances in coincidence time resolution for PET. Phys Med Biol. 2016 Mar; 61(6):2255–2264.

5. Yoon HS, Ko GB, Kwon SI, Lee CM, Ito M, Song IC, et al. Initial results of simultaneous PET/MRI experiments with an MRI-compatible silicon photomultiplier PET scanner. J Nucl Med. 2012 Apr; 53(4):608–614.

6. Ko GB, Yoon HS, Kim KY, Lee MS, Yang BY, Jeong JM, et al. Simultaneous multi-parametric PET/MRI with silicon photomultiplier PET and ultra-high field MRI for small animal imaging. J Nucl Med. 2016 Aug; 57(8):1309–1315.

7. Levin CS, Maramraju SH, Khalighi MM, Deller TW, Delso G, Jansen F. Design features and mutual compatibility studies of the time-of-flight PET capable GE SIGNA PET/MR system. IEEE Trans Med Imaging. 2016 Aug; 35(8):1907–1914.

8. Petasecca M, Alpat B, Ambrosi G, Azzarello P, Battiston R, Ionica M, et al. Thermal and electrical characterization of silicon photomultiplier. IEEE Trans Nucl Sci. 2008 Jun; 55(3):1686–1690.

9. Adamo G, Parisi A, Stivala S, Tomasino A, Agrò D, Curcio L, et al. Silicon photomultipliers signal-to-noise ratio in the continuous wave regime. IEEE J Sel Topics Quantum Electron. 2014 Nov; 20(6):3804907.

10. Bohn P, Clough A, Hazen E, Heering A, Rohlf J, Freeman J, et al. Radiation damage studies of silicon photomultipliers. Nucl Instrum Methods Phys Res A. 2009 Jan; 598(3):722–736.

11. NEMA standards publication NU2-2007. Performance measurements of positron emission tomographys. Rosslyn, VA: National Electrical Manufactureres Association; 2007.

12. Yamamoto S, Watabe H, Kato K, Hatazawa J. Performance comparison of high quantum efficiency and normal quantum efficiency photomultiplier tubes and position sensitive photomultiplier tubes for high resolution PET and SPECT detectors. Med Phys. 2012 Nov; 39(11):6900–6907.

13. Lee CM, Kwon SI, Ko GB, Ito M, Yoon HS, Lee DS, et al. A novel compensation method for the anode gain non-uniformity of multi-anode photomultiplier tubes. 2012 Jan; 57(1):191–207.

14. Kwon SI, Hong SJ, Ito M, Yoon HS, Lee GS, Sim KS, et al. Development of position encoding circuit for a multi-anode position sensitive photomultiplier tube. 2008 Dec; 42(6):469–477.

15. Won JY, Kwon SI, Yoon HS, Ko GB, Son J-W, Lee JS. Dual-phase tapped-delay-line time-to-digital converter with on-the-fly calibration implemented in 40 nm FPGA. IEEE Trans Biomed Circuits Syst. 2016 Feb; 10(1):231–242.

16. Yoon HS. Network based high performance data acquisition system for PET scanner. Ph. D. dissertation. Dept. Biomed. Sci., Seoul Natl. Univ., Seoul, Korea; 2015.

17. Son J-W, Lee MS, Lee JS. A depth-of-interaction PET detector using a stair-shaped reflector arrangement and a single-ended scintillation light readout. Phys Med Biol. 2017 Jan; 62(2):465–483.

18. Ito M, Lee JP, Lee JS. Timing performance study of new fast PMTs with LYSO for time-of-flight PET. IEEE Trans Nucl Sci. 2013 Feb; 60(1):30–37.

19. Peng Q, Choong WS, Moses WW. Evaluation of the timing properties of a high quantum efficiency photomultiplier tube. IEEE Trans Nucl Sci. 2013 Oct; 60(5):3212–3219.

20. Ko GB, Lee JS. Performance characterization of high quantum efficiency metal package photomultiplier tubes for time-of-flight and high-resolution PET applications. Med Phys. 2015 Jan; 42(1):510–520.

21. Nakazawa M, Ohi J, Tonami H, Yamada Y, Furumiya T, Furuta M, et al. Development of a prototype DOI-TOF-PET scanner. in Proc IEEE Nucl Sci Symp Med Imag Conf. 2010; 2077–2080.

22. Liu J-H, Cheng J-X, Xu J-H, Cheng F-F, Li D-W, Zhang Z-M, et al. Investigation of the time performance of a LYSO array for TOF-PET. Chinese Phys C. 2015 Dec; 39(12):128201.

23. Krishnamoorthy S, LeGeyt B, Werner ME, Kaul M, Newcorner FM, Karp JS et al. Design and performance of a high spatial resolution, time-of-flight PET detector. IEEE Trans Nucl Sci. 2014 Jan; 61(3):1092–1098.

24. Moses WW, Janecek M, Spurrier MA, Szupryszynski P, Choong W-S, Melcher CL, et al. Optimization of a LSO-based detector module for time-of-flight PET. IEEE Trans Nucl Sci. 2010 Jun; 57(3):1570–1576.

25. Peng Q, Choong W-S, Vu S, Huber JS, Janecek M, Wilson D, et al. Performance of the Tachyon Time-of-Flight PET Camera. IEEE Trans Nucl Sci. 2015 Feb; 62(1):111–119.

26. Daube-Witherspoon ME, Surti S, Perkins A, Kyba CCM, Wiener R, Werner ME, et al. The imaging performance of a LaBr3-based PET scanner. Phys Med Biol. 2010 Jan; 55(1):45–64.

27. Yoon HS, Lee JS. Bipolar analog signal multiplexing for position-sensitive PET block detectors. Phys Med Biol. 2014 Dec; 59(24):7835–7846.

28. Langen KM, Jones DTL. Organ motion and its management. Int J Rad Oncol Biol Phys. 2001 May; 50(1):265–278.

29. Surti S, Karp JS. Design considerations for a limited angle, dedicated breast, TOF PET scanner. Phys Med Biol. 2008 Jun; 53(11):2911–2921.

30. Tashima H, Yoshida E, Inadama N, Nishikido F, Nakajima Y, Wakizaka H, et al. Development of a small single-ring OpenPET prototype with a novel transformable architecture. Phys Med Biol. 2016 Feb; 61(4):1795–1809.

31. Rezaei A, Defrise M, Bal G, Michel C, Conti M, Watson C, et al. Simultaneous Reconstruction of Activity and Attenuation in Time-of-Flight PET. IEEE Trans Med Imaging. 2012 Dec; 31(12):2224–2233.

32. Rezaei A, Defrise M, Nuyts J. ML-reconstruction for TOF-PET with simultaneous estimation of the attenuation factors. IEEE Trans Med Imaging. 2014 Jul; 33(7):1563–1572.

33. Bettinardi V, Presotto L, Rapisarda E, Picchio M, Gianolli L, Gilardi MC. Physical Performance of the new hybrid PET/CT Discovery-690. Med Phys. 2011 Oct; 38(10):5394–5411.

34. Miller M, Zhang J, Binzel K, Griesmer J, Laurence T, Narayanan M, et al. Characterization of the Vereos Digital Photon Counting PET System. J Nucl Med. 2015 May; 56(suppl3):434.

35. Grant AM, Deller TW, Khalighi MM, Maramraju SH, Delso G, Levin CS. NEMA NU 2-2012 performance studies for the SiPM-based ToF-PET component of the GE SIGNA PET/MR system. Med Phys. 2016 May; 43(5):2334–2343.36.

36. Nemallapudi MV, Gundacker S, Lecoq P, Auffray E, Ferri A, Gola A, et al. Sub-100 ps coincidence time resolution for positron emission tomography with LSO:Ce codoped with Ca. Phys Med Biol. 2015 Jun; 60(12):4635–4649.

37. Turtos RM, Gundacker S, Polovitsyn A, Christodoulou S, Salomoni M, Auffray E, et al. Ultrafast emission from colloidal nanocrystals under pulsed X-ray excitation. J Instrum. 2016 Oct; 11:P10015.

38. Turtos RM, Gundacker S, Lucchini MT, Procházková L, Cuba V, Buresová H, et al. Timing performance of ZnO:Ga nanopowder composite scintillators. Phys Status Solidi RRL. 2016 Nov; 10(11):843–847.

39. Adamczewski-Musch J, Akishin P, Becker K-H, Belogurov S, Bendarouach J, Boldyreva N, et al. Single photon test bench for series tests of HAMAMATSU H12700 MAPMTs. Nucl Instrum Methods Phys Res A. 2017 Dec; 876:123–125.

40. Lecoq P, Auffray E, Knapitsch A. How photonic crystals can improve the timing resolution of scintillators. IEEE Trans Nucl Sci. 2013 Jun; 60(3):1653–1657.

41. Kurz C, Bauer J, Conti M, Guérin L, Eriksson L, Parodi K. Investigating the limits of PET/CT imaging at very low true count rates and high random fractions in ion-beam therapy monitoring. Med Phys. 2015 Jul; 42(7):3979–3991.

42. Chun SY, Kim KY, Lee JS, Fessler JA. Joint estimation of activity distribution and attenuation map for TOF-PET using alternating direction method of multiplier. in IEEE Int Symp Biomed Imaging. 2016; 86–89.

43. Ahn S, Kim SM, Son J, Lee DS, Lee JS. Gap compensation during PET image reconstruction by constrained, total variation minimization. Med Phys. 2012 Feb; 39(2):589–602.

국문 초록

생체 내의 생리적 현상을 분자 수준으로 촬영하는 것이 가능해짐에 따라 질병의 조기 진단이 가능해지고 있다. 양전자 방출 단층촬영기법(PET)은 이와 같은 분자 영상 기법 중 하나로, 체내에 주사한 방사성 의약품의 체내 분포를 추정함으로써 생리적 기능의 변화를 높은 민감도로 촬영하여 3 차원 영상으로 제공한다. 비정 시간 측정 가능 PET 장치는 영상의 품질을 향상시킴으로써 질병을 진단할 확률을 높이거나 환자의 촬영 시간 또는 방사선 피폭 정도를 감소시키는 효과를 나타내는 것으로 알려져 있다. 이에 본 연구에서는 고양자효율 다양극 광전자증배관을 이용하여 고성능의 비정 시간 측정 PET 프로토타입을 개발하였다. 다양한 팬텀 촬영을 수행한 결과 이 프로토타입은 우수한 시간 성능과 향상된 영상을 제공함을 확인하였다. 본 시스템을 활용하여 우수한 시간 성능이 갖는 장점을 실험적으로 입증할 수 있음과 기술적인 한계로 적용이 불가능했던 새로운 PET 응용 분야의 실현 가능성 평가가 가능함을 확인하였다.